Microscopic picture of paraelectric perovskites from structural prototypes

Michele Kotiuga [1,*] Samed Halilov,[2] Boris Kozinsky,[3,4] Marco Fornari [5] Nicola Marzari [1] and Giovanni Pizzi [1,†]

[1]*Theory and Simulation of Materials (THEOS), National Centre for Computational Design and Discovery of Novel Materials (MARVEL), École Polytechnique Fédérale de Lausanne, CH-1015 Lausanne, Switzerland*
[2]*Designed Material Technologies, LLC, P.O. Box 14548, Richmond, Virginia 23221-9998, USA*
[3]*John A. Paulson School of Engineering and Applied Sciences, Harvard University, 29 Oxford Street, Cambridge, Massachusetts 02138, USA*
[4]*Robert Bosch LLC, Research and Technology Center, Cambridge, Massachusetts 02139, USA*
[5]*Department of Physics and Science of Advanced Materials Program, Central Michigan University, Mt. Pleasant, Michigan 48859, USA*

We highlight with first-principles molecular dynamics the persistence of intrinsic $\langle 111 \rangle$ Ti off-centerings for BaTiO$_3$ in its cubic paraelectric phase. Intriguingly, these are inconsistent with the $Pm\bar{3}m$ space group often used to atomistically model this phase using density-functional theory or similar methods. Therefore, we deploy a systematic symmetry analysis to construct representative structural models in the form of supercells that satisfy a desired point symmetry but are built from the combination of lower-symmetry primitive cells. We define as structural prototypes the smallest of these that are both energetically and dynamically stable. Remarkably, two 40-atom prototypes can be identified for paraelectric BaTiO$_3$; these are also common to many other ABO$_3$ perovskites. These prototypes can offer structural models of paraelectric phases that can be used for the computational engineering of functional materials. Last, we show that the emergence of B-cation off-centerings and the primitive-cell phonon instabilities is controlled by the equilibrium volume, in turn, dictated by the filler A cation.

Compounds with the perovskite structure are a versatile class of functional materials exhibiting a wide range of properties, such as superconductivity [1], catalysis [2], photovoltaic energy harvesting [3], and ferroelectricity [4,5]. When ferroelectric, perovskites sustain a spontaneous polarization that can be switched with an electric field; as the temperature is raised, there is a transition above the Curie temperature to a paraelectric phase that has no net polarization. Early studies of BaTiO$_3$ (a prototypical ABO$_3$ ferroelectric perovskite) suggested for these transitions a microscopic "displacive" model in which local displacements of the B cation (titanium) align with the macroscopic polarization [6,7]. For BaTiO$_3$, this is along the $\langle 111 \rangle$ direction in the rhombohedral ground state; as the temperature increases there is a transition to an orthorhombic phase above 183 K with the polarization along $\langle 110 \rangle$, then to a tetragonal phase above 278 K with the polarization along $\langle 100 \rangle$, before reaching the paraelectric cubic phase above 393 K with no net polarization [7]. The results from diffuse x-ray scattering for all phases but the rhombohedral one [8,9] are somewhat inconsistent with such a displacive model. This has led to the application of the order-disorder model for the transitions [10,11] in which local polar displacements, driven by the pseudo-Jahn-Teller effect [12], are in different ordered arrangements in the ferroelectric phases at low temperatures and become disordered in the paraelectric phase. These two models can be reconciled if one considers the time averaging inherent to most characterization techniques, which can effectively wash out the local displacements and present a higher-symmetry structure where the averaged displacements are aligned with the macroscopic polarization or cancel out [13].

Microscopic displacements [8,9,13–19] and phase transitions in perovskites have been studied extensively using effective Hamiltonians [20–25] or molecular dynamics, most often based on density-functional theory (DFT) [26–31]. Interestingly, BaTiO$_3$ supercells possessing local $\langle 111 \rangle$ Ti displacements and maintaining the experimentally observed macroscopic polarization have been shown to be energetically favorable [32–34] and dynamically stable [32], offering a unique insight into the microscopic potential-energy surfaces for these materials.

To elucidate the microscopic picture of paraelectricity in these perovskites, we performed Car-Parrinello molecular dynamics (CPMD) simulations of cubic BaTiO$_3$, finding clear microscopic evidence of Ti off-centerings, and associated dipoles along the $\langle 111 \rangle$ directions which persist well above the Curie temperature, consistent with the order-disorder model.

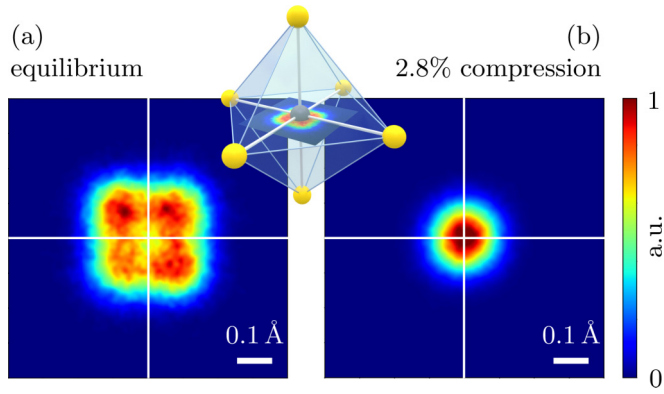*michele.kotiuga@epfl.ch
†giovanni.pizzi@epfl.ch

(a) equilibrium   (b) 2.8% compression

FIG. 1. CPMD simulation of $BaTiO_3$. Histograms of the xy-plane projection of the displacement of Ti atoms with respect to the barycenter of the surrounding TiO_6 octahedron at (a) equilibrium volume (lattice parameter: 4.00 Å) and (b) under a 2.8% compressive hydrostatic strain (lattice parameter: 3.89 Å), integrated over 13 ps of fixed-volume NVE CPMD simulations and on all Ti atoms of a $4 \times 4 \times 4$ cubic supercell. The average temperature of the simulation is 315 K. The inset: graphical three-dimensional representation depicting the xy-plane projection of the Ti cation position in a representative TiO_6 octahedron.

This is clearly apparent in Fig. 1(a), where we present the results of CPMD simulations at 315 K for a $4 \times 4 \times 4$ cubic supercell; the histogram for the Ti displacements projected onto one of the equivalent [100] planes shows how the Ti atoms always occupy off-center $\langle 111 \rangle$ positions, rather than sitting at the center of their surrounding oxygen octahedron [35] (for the Methodology see the Supplemental Material (SM) Sec. 1 [36]; for the associated data, see Ref. [37] on the Materials Cloud [38]). We observe these off-center displacements up to temperatures around 450 K; furthermore, they can be suppressed with compressive hydrostatic strain, resulting in an isotropic distribution [Fig. 1(b)] in agreement with experimental measurements [39,40]. This observation will be relevant to the later discussion of volume effects and the role of A-site cations.

Inspired by these results, we aim here to systematically explore the microscopic structure of the paraelectric phase of $BaTiO_3$, to extend this exploration to other perovskites, and to lay the groundwork for a systematic analysis of phases that can possess "hidden order," including other ferroelectric or magnetic systems [41–43] or those displaying higher-order couplings [44]. With this goal in mind, we introduce first the concept of microscopic templates, defined as lower-symmetry supercells that preserve a desired point symmetry (e.g., cubic). We then define microscopic prototypes as the smallest of these templates that are both energetically and dynamically stable (i.e., lower in energy, per formula unit, than the higher-symmetry primitive cell and with real positive phonon dispersions), thus, identifying the highest-symmetry stable structures possessing the requisite symmetry while minimizing the computational cost. This approach is distinct yet complementary to that of special quasirandom structures (SQSs) when used to describe a polymorphous network in which a single large SQS exhibiting many local motifs is used. In this context, slightly different from

TABLE I. The microscopic templates derived from the cubic subgroups (up to a $2 \times 2 \times 2$ supercell) of parent-group $Pm\bar{3}m$ (221) with, at least, one degree of freedom for the $1b$ Wyckoff position, allowing for B-site off-centering. We list the subgroup (international short symbol and number in parentheses), the subgroup index, and the splittings of the three relevant Wyckoff positions ($1a$, $1b$, and $3c$). These cells are a $2 \times 2 \times 2$ supercell of the primitive cell with no translation.

Group		Index	$1a$	$1b$	$3c$
$Pm\bar{3}m$	(221)	8	$1a\ 1b\ 3c\ 3d$	$8g$	$12i\ 12j$
$P\bar{4}3n$	(218)	16	$2a\ 6b$	$8e$	$24i$
$I\bar{4}3m$	(217)	8	$2a\ 6b$	$8c$	$24g$
$P\bar{4}3m$	(215)	16	$1a\ 1b\ 3c\ 3d$	$4e\ 4e$	$12i\ 12i$
$Pa\bar{3}$	(205)	16	$4a\ 4b$	$8c$	$24d$
$Pm\bar{3}$	(200)	16	$1a\ 1b\ 3c\ 3d$	$8i$	$12j\ 12k$
$I2_13$	(199)	16	$8a$	$8a$	$12b\ 12b$
$P2_13$	(198)	32	$4a\ 4a$	$4a\ 4a$	$12b\ 12b$
$I23$	(197)	16	$2a\ 6b$	$8c$	$24f$
$P23$	(195)	32	$1a\ 1b\ 3c\ 3d$	$4e\ 4e$	$12j\ 12j$

the original development of SQSs to characterize disordered alloys with first-principles calculations [45,46], SQSs have been recently used to study paramagnetic phases [47,48] and complex perovskite-based systems [34,49–52]. In this paper we develop instead a symmetry-based analysis and workflow, enumerating all possible supercells (up to a given size) with a desired point symmetry. In this way we identify not just local motifs, but more complex orderings which respect the desired global point symmetry. We describe it in the following and apply to structural microscopic prototypes, but these concepts can be equally applied to magnetic or electronic prototypes.

To identify structural prototypes we use group-subgroup relations as discussed in Ref. [53] to systematically enumerate all microscopic templates; here, we take the case of the cubic ABO_3 perovskite with space-group $Pm\bar{3}m$ (international number 221) where the $1a$, $1b$, and $3c$ Wyckoff positions are occupied by the A, B, and O atoms, respectively. For each cubic subgroup of $Pm\bar{3}m$, we define a cubic microscopic template as a supercell that can host symmetry-allowed displacements of A, B, and O atoms relative to their positions in the high-symmetry parent structure (group $Pm\bar{3}m$) with no net polarization (see SM Sec. 1 [36] for further details). Using $2 \times 2 \times 2$ supercells of 40 atoms, we find 27 distinct cubic microscopic templates of group $Pm\bar{3}m$, 10 of which host only oxygen displacements, whereas the remaining 17 allow the A and/or B cations to displace as well. Table I summarizes the subgroups in which the B cations can displace; see SM Secs. 2 and 3 [36] for the complete list as well as a list duplicates that correspond to microscopic templates with higher symmetry. The same analysis can be applied to supercells of any desired size, but we find that in $BaTiO_3$ these $2 \times 2 \times 2$ supercells are already sufficient to identify structural prototypes.

We then determine which of these microscopic templates, if any, are energetically stable. Using variable-cell first-principles relaxations performed with QUANTUM ESPRESSO [55,56] using the revised Perdew-Burke-Enzerhof functional for solids (PBEsol) [57] and managed with AiiDA [58–60], we take these $2 \times 2 \times 2$ templates as starting
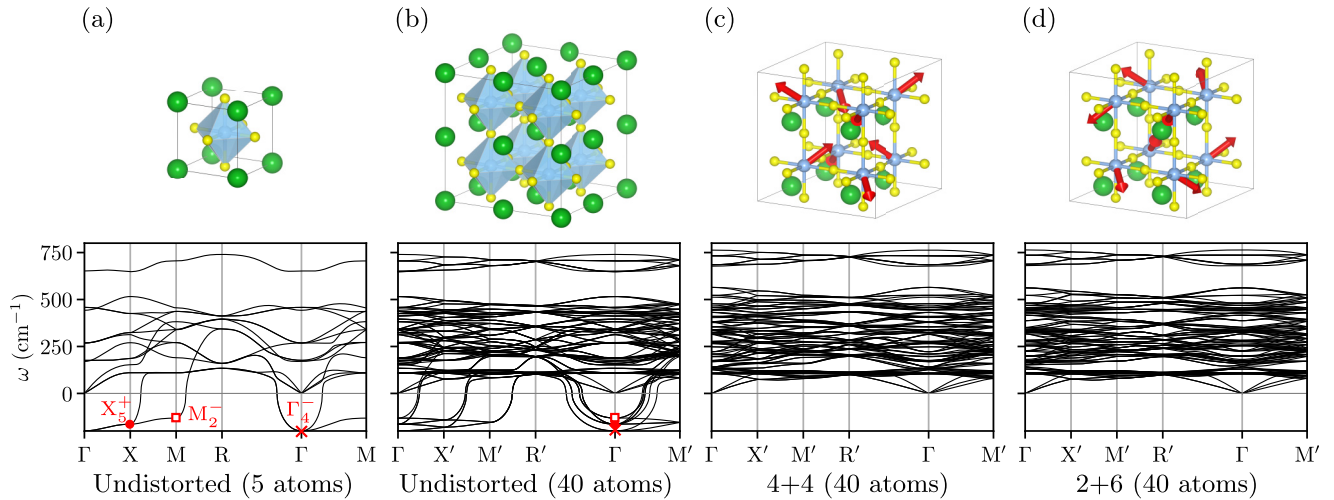
FIG. 2. Crystal structures (top) and phonon dispersions (bottom) for various BaTiO$_3$ cells with Ba, Ti, and O atoms shown in green, blue, and yellow, respectively. (a) Five-atom primitive cubic cell (standard crystallographic labels from Ref. [54]), displaying unstable phonon modes. The high-symmetry Γ_4^-, X_5^+, and M_2^- instabilities are marked in red with a cross, a filled circle, and an empty square, respectively. (b) Forty-atom undistorted supercell; X', M' and R' labels indicate the X, M, and R points of the $2 \times 2 \times 2$ supercell, respectively [the same labels are used also in panels (c) and (d)]. All three instabilities marked in panel a fold at Γ in this supercell. Forty-atom supercells of the (c) 4+4 and (d) 2+6 displacement patterns. In panels (c) and (d) (top), red arrows indicate the direction of atomic displacements (only shown for B cations for clarity). We refer the reader to the SM Sec. 5 [36] for the displacement pattern associated with each unstable mode and the other modes that contribute to the 4 + 4 and 2 + 6 displacement patterns, which can also be visualized with the interactive phonon visualizer tool on the Materials Cloud [38].

structures and require that the point symmetry remains cubic (see SM Sec. 1 [36] for further details). Remarkably, we find that two of the microscopic templates relax to supercells with nontrivial displacement patterns of the B cations; moreover, they display stable phonon dispersions across the entire Brillouin zone [Figs. 2(c) and 2(d)]. The remaining 25 templates either relax back to (the $2 \times 2 \times 2$ supercell of) the five-atom primitive cell, well-known to be dynamically unstable [Figs. 2(a) and 2(b)] [61,62] or to one of these two non-trivial displacement patterns. These energetically and dynamically stable structures are the structural prototypes. As they are locally stable structures of the 0 K potential-energy landscape they serve as minimal models possessing the signature of the paraelectric phase, namely a global cubic symmetry but with local Ti displacements. These displacements, driven by local chemistry, can then also acquire correlations (e.g. linear chains [8]) that can be studied with large-scale molecular dynamics simulations [27,30,63].

The two structural prototypes have symmetry $I\bar{4}3m$ and $Pa\bar{3}$, respectively (see Table I); their structure and B-atom (Ti) displacement patterns are shown in Figs. 2(c) and 2(d). We name these two prototypes 4 + 4 and 2 + 6 (for $I\bar{4}3m$ and $Pa\bar{3}$, respectively), since considering any Ba atom, in the 4 + 4 (2 + 6) structure there are 4 (2) surrounding Ti atoms that displace toward it, while the remaining 4 (6) displace outwards. We note that the 4 + 4 structure ($I\bar{4}3m$) has been previously discussed in the work of Zhang *et al.* [32]. The 4 + 4 and the 2 + 6 structural prototypes are lower in energy than the undistorted cubic structure by 11 and 15 meV/formula unit, respectively. Furthermore, there is an energy barrier of only 3 meV/formula unit between these two structural prototypes (as found by nudged-elastic-band calculations, see

SM Sec. 4 [36]), suggesting that thermal fluctuations of the off-centerings do not require to go through the high-symmetry structure.

We contrast the phonon dispersions of the high-symmetry structure [Figs. 2(a) and 2(b)] with that of the two prototypes [Figs. 2(c) and 2(d)]. The five-atom primitive cell displays instabilities at the zone-center Γ, belonging to the irreducible representation (irrep) Γ_4^-, and at the zone-boundary points X and M (irreps X_5^+ and M_2^-, respectively). To gain further insight into the 4 + 4 and 2 + 6 patterns we analyze these with respect to the irreps of the five-atom-cell phonons using the ISODISTORT software [64,65]. We find that the displacements of both prototypes contain a mode with the symmetry of an unstable zone-boundary mode. Specifically, the 4 + 4 prototype can be constructed by adding the displacements having the symmetry of the M_2^- and M_1^+ irreps, whereas the 2 + 6 prototype originates from the X_5^+ and M_5^+ irreps (see SM Fig. S2 [36] for the M_1^+ and M_5^+ modes). Most importantly, out of the 27 distinct cubic templates, the 4 + 4 ($I\bar{4}3m$) and 2 + 6 ($Pa\bar{3}$) are the only ones with a displacement pattern that is constructed, in part, from a mode with the symmetry of an unstable mode of the parent structure, resulting in an appealing one-to-one correspondence between unstable zone-boundary phonon modes and prototypes with stable displacement patterns in $2 \times 2 \times 2$ cubic supercells. We note that the displacement patterns must occur in combination with another mode in a cubic structure as they do not possess a cubic point symmetry. Furthermore, the Γ_4^- mode is the polar instability and can only occur in lower-symmetry polar phases of BaTiO$_3$, which are, therefore, noncubic.

We investigate in more detail the zone-boundary modes and the stability of the structural prototypes as a function of
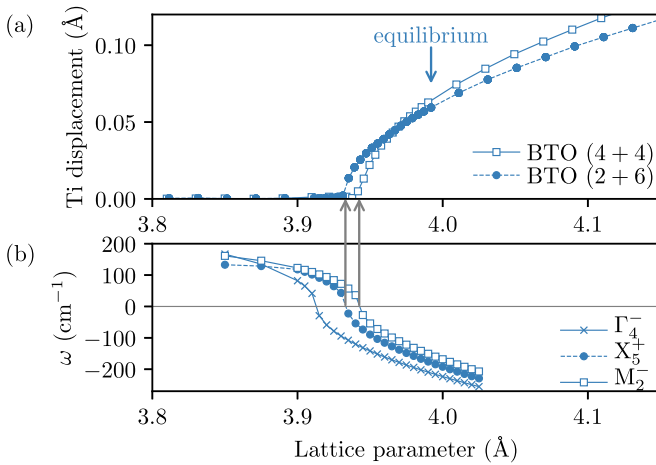
FIG. 3. (a) Magnitude of the Ti-atom displacements for the $4 + 4$ and $2 + 6$ patterns in BaTiO$_3$ as a function of the lattice parameter. Displacements are along the $\langle 111 \rangle$ directions, and we plot the displacement in angstrom along one Cartesian coordinate. The DFT (PBEsol) equilibrium lattice parameter in its lowest-energy cubic configuration is indicated by the blue arrow. (b) Plot of the unstable phonon modes of BaTiO$_3$ with irrep Γ_4^-, X_5^+, and M_2^- in the five-atom undistorted cubic cell as a function of the lattice parameter. The gray arrows indicate the lattice parameters at which the modes at X and M become unstable; they are in agreement with the corresponding displacement onsets in panel (a).

FIG. 4. Magnitude of the Ti-atom displacements for the $4 + 4$ pattern in (Ba, Pb, Sr, Ca)TiO$_3$ (labeled as BTO, PTO, STO, and CTO) as a function of the lattice parameter. Displacements are along the $\langle 111 \rangle$ directions, and we plot the displacement in angstrom along one Cartesian coordinate. The DFT (PBEsol) equilibrium lattice parameter is indicated by the arrow of the corresponding color. A clear universal trend across the titanates is demonstrated; the $4 + 4$ pattern is stable only in unstrained BaTiO$_3$ because of the larger A cation and, thus, larger lattice parameter.

volume, prompted by the disappearance of the Ti off-centering under pressure in our CPMD simulations [Fig. 1(b)] and in experiments [39,40]. We find that with increasing pressure the magnitude of the Ti displacements decreases for both prototypes and disappears when the lattice parameter is reduced by $\approx 1.6\%$ as reported in Fig. 3(a). We find that the Ti displacements as a function of volume can be fit by a double-well potential where the quadratic coefficient depends linearly on volume and changes sign at the onset of the displacements (see SM Sec. 6 [36]). This suggests that, at least, one phonon mode associated with this structural prototype becomes unstable at the same volume where the Ti displacement becomes energetically favorable. In Fig. 3(b) we plot as a function of the lattice parameter the phonon frequencies for the $q = \Gamma$, X, and M modes that are unstable in the five-atom primitive cell (irreps Γ_4^-, X_5^+, and M_2^-, respectively). We find that expanding the volume further softens these modes, whereas applying pressure stabilizes them, in agreement with previous calculations [66]. The fact that the Γ_4^- mode also stabilizes at a lower lattice parameter is indicative of a pressure at which the system could be ferroelectric below a critical temperature, but no Ti displacements would be observed in the cubic paraelectric phase. Notably, the M_2^- and X_5^+ modes become unstable at the same lattice parameter where the $4 + 4$ and $2 + 6$ displacement patterns, respectively, emerge [gray arrows in Fig. 3(b)].

Thus, the $4 + 4$ and $2 + 6$ prototypes originate from the unstable M_2^- and X_5^+ modes, which do not involve A-cation displacements. To test the effect of the A cation we extend the study to PbTiO$_3$, SrTiO$_3$, and CaTiO$_3$. We report in Fig. 4 the results for the $4 + 4$ prototype, highlighting a universal trend where the B-site displacement as a function of lattice
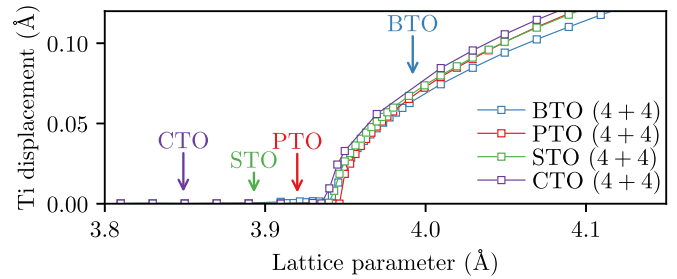
parameter is broadly independent of the chosen A cation. The stability of the prototype, and, thus, the nature of the paraelectric phase, is instead determined by the equilibrium lattice parameter—indicated in Fig. 4 by arrows—which is largely determined by the A cation. For Pb, Sr, and CaTiO$_3$ the lattice parameter is smaller than the critical value at which the displacement pattern becomes energetically favorable, ~ 3.95 Å. For all titanates studied, the displacement pattern onset occurs at the lattice parameter at which the M_2^- mode becomes unstable. A similar picture emerges for the $2 + 6$ pattern (except for CaTiO$_3$, due to its significantly smaller lattice parameter)—see SM Sec. 7 [36].

Testing a broader range of 49 perovskites from Ref. [67] shows that B-site off-centerings along $\langle 111 \rangle$ directions provide prototypes at the relaxed equilibrium lattice parameter not only for BaTiO$_3$, but for most zirconates, niobates, tantalates, CaHfO$_3$, and BiScO$_3$ as reported in SM Sec. 8 [36]. However, the energetic stability of these prototypes as a function of lattice parameter is B-site specific. This is expanded on in SM Sec. 9 [36] where we further investigate the stability of the $4 + 4$ and $2 + 6$ displacement patterns as a function of lattice parameter in the titanates, niobates, and zirconates, demonstrating the universality of the occurrence of B-cation displacements and their strong, family-specific volume dependence.

The relationship we have observed between the unstable zone-boundary phonons of the primitive cubic structure and the displacement patterns as a function of lattice parameter indicates that, at a given volume, one could use the unstable phonon modes to predict which microscopic templates would result in structural prototypes. To verify the robustness of our conclusions against the choice of DFT functional, we tested for BaTiO$_3$ the dependence on the functional, finding that the Ti displacement amplitudes are independent of the functional choice (see SM Sec. 10 [36]), but that the functional determines the equilibrium volume. This highlights the need to choose a functional that accurately reproduces the experimental lattice parameter in order to correctly predict which prototypes occur at the equilibrium volume.

To summarize, motivated by the observed persistence of $\langle 111 \rangle$ Ti off-centerings above the Curie temperature in our CPMD simulations of BaTiO$_3$, we systematically identify microscopic structural prototypes of the paraelectric phase, i.e., the smallest supercells with cubic point symmetry that are simultaneously energetically and dynamically stable. These cubic prototypes, hosting stable local dipoles due to the $\langle 111 \rangle$ Ti displacements in a cubic paraelectric phase, are found through a symmetry analysis exploring all possible 40-atom microscopic templates, followed by density-functional theory and density-functional perturbation theory calculations to assess energetic and dynamical stability. Moreover, we highlight how off-centering amplitudes are strongly dependent on volume and relate their patterns to the zone-boundary unstable phonons of the five-atom undistorted primitive cubic cell, suggesting a predictor for the identification of such prototypes. These cubic prototypes would be challenging to identify without the present symmetry-based approach due to the combinatorial complexity of large supercells and the attractive basin of the rhombohedral five-atom ground state associated with the polar instability. We highlight that these prototypes can serve as minimal models of the paraelectric phase in first-principles calculations of response functions with the correct tensorial symmetry as they provide a faithful microscopic representation with key features: the persistence of local Ti displacements and the appropriate macroscopic point group.

We finally emphasize that this approach is general. Beyond its extension to study the prevalence of the *B*-site $\langle 111 \rangle$ off-centerings in *AB*O$_3$ perovskites, it can be used in any crystalline system to find candidate templates and efficiently search for prototypes that are local minima in the potential-energy surface, providing an in-depth study of, for example, the electronic or magnetic properties of a polymorphic system. This approach lays the foundation to investigate dynamics, thermodynamics, and chemical substitutions as these prototypes could be used to capture subtle details of the energy landscape and to provide models to study the properties or transitions of disordered phases, such as alloys, paramagnetic phases, or defects in paraelectric phases.

---

[1] J. G. Bednorz and K. A. Müller, Perovskite-type oxides—the new approach to high-T_c superconductivity, Rev. Mod. Phys. **60**, 585 (1988).

[2] J. Hwang, R. R. Rao, L. Giordano, Y. Katayama, Y. Yu, and Y. Shao-Horn, Perovskites in catalysis and electrocatalysis, Science **358**, 751 (2017).

[3] A. K. Jena, A. Kulkarni, and T. Miyasaka, Halide perovskite photovoltaics: Background, status, and future prospects, Chem. Rev. **119**, 3036 (2019).

[4] F. Jona and G. Shriane, *Ferroelectric Crystals* (Dover, New York, 1962)

[5] M. E. Lines and A. M. Glass, *Principles and Applications of Ferroelectrics and Related Materials* (Clarendon, Oxford, 1977).

[6] A. von Hippel, R. G. Breckenridge, F. G. Chesley, and L. Tisza, High dielectric constant ceramics, Ind. Eng. Chem. **38**, 13 (1946).

[7] W. J. Merz, The electric and optical behavior of BaTiO$_3$ single-domain crystals, Phys. Rev. **76**, 1221 (1949).

[8] R. Comès, M. Lambert, and A. Guinier, The chain structure of BaTiO$_3$ and KNbO$_3$, Solid State Commun. **6**, 715 (1968).

[9] R. Comès, M. Lambert, and A. Guinier, Désordre linéaire dans les cristaux (cas du silicium, du quartz, et des pérovskites ferroélectriques), Acta Crystallogr., Section A: Cryst. Phys., Diffr. Theor. Gen. Crystallogr. **26**, 244 (1970).

[10] I. B. Bersuker, On the origin of ferroelectricity in perovskite-type crystals, Phys. Lett. **20**, 589 (1966).

[11] A. S. Chaves, F. C. S. Barreto, R. A. Nogueira, and B. Zẽks, Thermodynamics of an eight-site order-disorder model for ferroelectrics, Phys. Rev. B **13**, 207 (1976).

[12] I. B. Bersuker, Pseudo-Jahn–Teller effect—A two-state paradigm in formation, deformation, and transformation of molecular systems and solids, Chem. Rev. **113**, 1351 (2013).

[13] E. A. Stern, Character of Order-Disorder and Displacive Components in Barium Titanate, Phys. Rev. Lett. **93**, 037601 (2004).

[14] B. Ravel, E. A. Stern, R. I. Vedrinskii, and V. Kraizman, Local structure and the phase transitions of BaTiO$_3$, Ferroelectrics **206**, 407 (1998).

[15] B. Zalar, V. V. Laguta, and R. Blinc, NMR Evidence for the Coexistence of Order-Disorder and Displacive Components in Barium Titanate, Phys. Rev. Lett. **90**, 037601 (2003).

[16] I. Levin, V. Krayzman, and J. C. Woicik, Local structure in perovskite (Ba, Sr)TiO$_3$: Reverse Monte Carlo refinements from multiple measurement techniques, Phys. Rev. B **89**, 024106 (2014).

[17] M. S. Senn, D. A. Keen, T. C. A. Lucas, J. A. Hriljac, and A. L. Goodwin, Emergence of Long-Range Order in BaTiO$_3$ from Local Symmetry-Breaking Distortions, Phys. Rev. Lett. **116**, 207602 (2016).

[18] C. Shi, S. J. L. Billinge, E. Puma, S. H. Bang, N. J. H. Bean, J.-C. de Sugny, R. G. Gambee, R. C. Haskell, A. Hightower, and T. C. Monson, Barium titanate nanoparticles: Short-range lattice distortions with long-range cubic order, Phys. Rev. B **98**, 085421 (2018).

[19] A. Bencan, E. Oveisi, S. Hashemizadeh, V. K. Veerapandiyan, T. Hoshina, T. Rojac, M. Deluca, G. Drazic, and D. Damjanovic, Atomic scale symmetry and polar nanoclusters in the paraelectric phase of ferroelectric materials, Nat. Commun. **12**, 3509 (2021).

[20] W. Zhong, D. Vanderbilt, and K. M. Rabe, Phase Transitions in BaTiO$_3$ from First Principles, Phys. Rev. Lett. **73**, 1861 (1994).

[21] W. Zhong, D. Vanderbilt, and K. M. Rabe, First-principles theory of ferroelectric phase transitions for perovskites: The case of BaTiO$_3$, Phys. Rev. B **52**, 6301 (1995).

[22] Y. Girshberg and Y. Yacoby, Ferroelectric phase transitions and off-centre displacements in systems with strong electron-phonon interaction, J. Phys.: Condens. Matter **11**, 9807 (1999).

[23] H. Fu and L. Bellaiche, Ferroelectricity in Barium Titanate Quantum Dots and Wires, Phys. Rev. Lett. **91**, 257601 (2003).

[24] R. Pirc and R. Blinc, Off-center Ti model of barium titanate, Phys. Rev. B **70**, 134107 (2004).

[25] L. Walizer, S. Lisenkov, and L. Bellaiche, Finite-temperature properties of (Ba,Sr)TiO$_3$ systems from atomistic simulations, Phys. Rev. B **73**, 144105 (2006).

[26] H. Krakauer, R. Yu, C.-Z. Wang, K. M. Rabe, and U. V. Waghmare, Dynamic local distortions in KNbO$_3$, J. Phys.: Condens. Matter **11**, 3779 (1999).

[27] I. Ponomareva, L. Bellaiche, T. Ostapchuk, J. Hlinka, and J. Petzelt, Terahertz dielectric response of cubic BaTiO$_3$, Phys. Rev. B **77**, 012102 (2008).

[28] T. Nishimatsu, U. V. Waghmare, Y. Kawazoe, and D. Vanderbilt, Fast molecular-dynamics simulation for ferroelectric thin-film capacitors using a first-principles effective hamiltonian, Phys. Rev. B **78**, 104104 (2008).

[29] Y. Qi, S. Liu, I. Grinberg, and A. M. Rappe, Atomistic description for temperature-driven phase transitions in BaTiO$_3$, Phys. Rev. B **94**, 134308 (2016).

[30] M. Paściak, T. R. Welberry, J. Kulda, S. Leoni, and J. Hlinka, Dynamic Displacement Disorder of Cubic BaTiO$_3$, Phys. Rev. Lett. **120**, 167601 (2018).

[31] L. Chen, B. Xu, Y. Yang, and L. Bellaiche, Macroscopic and microscopic structures of cesium lead iodide perovskite from atomistic simulations, Adv. Funct. Mater. **30**, 1909496 (2020).

[32] Q. Zhang, T. Cagin, and W. A. Goddard, The ferroelectric and cubic phases in BaTiO$_3$ ferroelectrics are also antiferroelectric, Proc. Natl. Acad. Sci. USA **103**, 14695 (2006).

[33] Z. Wang, O. I. Malyi, X. Zhao, and A. Zunger, Mass enhancement in 3d and s-p perovskites from symmetry breaking, Phys. Rev. B **103**, 165110 (2021).

[34] X.-G. Zhao, O. I. Malyi, S. J. L. Billinge, and A. Zunger, Intrinsic local symmetry-breaking in nominally cubic paraelectric BaTiO$_3$, arXiv:2106.05231.

[35] We stress here that as we refer to different supercell sizes throughout this paper, we use the term lattice parameter to indicate the average lattice parameter of an equivalent five-atom primitive cell, e.g., the actual supercell lattice parameter divided by 4 for a 4×4×4 supercell.

[36] See Supplemental Material at http://link.aps.org/supplemental/10.1103/PhysRevResearch.4.L012042 for additional details regarding the methodology, subgroups, NEB calculations, phonons, and template stability.

[37] M. Kotiuga, S. Halilov, B. Kozinsky, M. Fornari, N. Marzari, and G. Pizzi, A microscopic picture of paraelectric perovskites from structural prototypes, Materials Cloud Archive **2022.32** (2022), doi: 10.24435/materialscloud:jc-ky.

[38] L. Talirz, S. Kumbhar, E. Passaro, A. R. V. Yakutovich, V. Granata, G. Fernando, M. Borelli, M. N. Uhrin, S. P. Huber, Z. Spyros *et al.*, Materials cloud, a platform for open computational science, Sci. Data **7**, 299 (2020).

[39] D. L. Decker and Y. X. Zhao, Dielectric and polarization measurements on BaTiO$_3$ at high pressures to the tricritical point, Phys. Rev. B **39**, 2432 (1989).

[40] J. P. Itié, B. Couzinet, A. Polian, A. M. Flank, and P. Lagarde, Pressure-induced disappearance of the local rhombohedral distortion in BaTiO$_3$, Europhys. Lett. **74**, 706 (2006).

[41] X. Zhang, Q. Liu, J.-W. Luo, A. J. Freeman, and A. Zunger, Hidden spin polarization in inversion-symmetric bulk crystals, Nat. Phys. **10**, 387 (2014).

[42] L. Yuan, Q. Liu, X. Zhang J.-W. Luo, S.-S. Li, and A. Zunger, Uncovering and tailoring hidden rashba spin–orbit splitting in centrosymmetric crystals, Nat. Commun. **10**, 906 (2019).

[43] R. Zhang, A. Marrazzo, N. Verstraete, N. Marzari, and T. Sohier, Gate control of spin-layer-locking FETs and application to monolayer LuIO, Nano Letters **21**, 7631 (2021).

[44] G. Aeppli, A. V. Balatsky, H. M. Rønnow, and N. A. Spaldin, Hidden, entangled and resonating order, Nat. Rev. Mater. **5**, 477 (2020).

[45] A. Zunger, S.-H. Wei, L. G. Ferreira, and J. E. Bernard, Special Quasirandom Structures, Phys. Rev. Lett. **65**, 353 (1990).

[46] A. van de Walle, P. Tiwary, M. de Jong, D. L. Olmsted, M. Asta, A. Dick, D. Shin, Y. Wang, L. Q. Chen, and Z. K. Liu, Efficient stochastic generation of special quasirandom structures, Calphad: Comput. Coupling Phase Diagrams Thermochem. **42**, 13 (2013).

[47] F. Körmann, A. Dick, B. Grabowski, T. Hickel, and J. Neugebauer, Atomic forces at finite magnetic temperatures: Phonons in paramagnetic iron, Phys. Rev. B **85**, 125104 (2012).

[48] G. Trimarchi, Z. Wang, and A. Zunger, Polymorphous band structure model of gapping in the antiferromagnetic and paramagnetic phases of the Mott insulators MnO, FeO, CoO, and NiO, Phys. Rev. B **97**, 035107 (2018).

[49] A. I. Lebedev, Ab initio studies of dielectric, piezoelectric, and elastic properties of BaTiO$_3$/SrTiO$_3$ ferroelectric superlattices, Phys. Solid State **51**, 2324 (2009).

[50] B. K. Voas, T.-M. Usher, X. Liu, S. Li, J. L. Jones, X. Tan, V. R. Cooper, and S. P. Beckman, Special quasirandom structures to study the (K$_{0.5}$Na$_{0.5}$)NbO$_3$ random alloy, Phys. Rev. B **90**, 024105 (2014).

[51] J. Varignon, M. Bibes, and A. Zunger, Origin of band gaps in 3d perovskite oxides, Nat. Commun. **10**, 1658 (2019).

[52] X.-G. Zhao, G. M. Dalpian, Z. Wang, and A. Zunger, Polymorphous nature of cubic halide perovskites, Phys. Rev. B **101**, 155137 (2020).

[53] B. Kozinsky, S. A. Akhade, P. Hirel, A. Hashibon, C. Elsässer, P. Mehta, A. Logeat, and U. Eisele, Effects of Sublattice Symmetry and Frustration on Ionic Transport in Garnet Solid Electrolytes, Phys. Rev. Lett. **116**, 055901 (2016).

[54] Y. Hinuma, G. Pizzi, Y. Kumagai, F. Oba, and I. Tanaka, Band structure diagram paths based on crystallography, Comput. Mater. Sci. **128**, 140 (2017).

[55] P. Giannozzi, S. Baroni, N. Bonini, M. Calandra, R. Car, C. Cavazzoni, D. Ceresoli, G. L. Chiarotti, M. Cococcioni, I. Dabo *et al.*, Quantum espresso: a modular and open-source software project for quantum simulations of materials, J. Phys.: Condens. Matter **21**, 395502 (2009).

[56] P. Giannozzi, O. Andreussi, T. Brumme, O. Bunau, M. B. Nardelli, M. Calandra, R. Car, C. Cavazzoni, D. Ceresoli, M. Cococcioni *et al.*, Advanced capabilities for materials modelling with quantum espresso, J. Phys.: Condens. Matter **29**, 46 (2017).

[57] J. P. Perdew, A. Ruzsinszky, G. I. Csonka, O. A. Vydrov, G. E. Scuseria, L. A. Constantin, X. Zhou, and K. Burke, Restoring the Density-Gradient Expansion for Exchange in Solids and Surfaces, Phys. Rev. Lett. **100**, 136406 (2008).

[58] G. Pizzi, A. Cepellotti, R. Sabatini, N. Marzari, and B. Kozinsky, AiiDA: Automated interactive infrastructure and database for computational science, Comput. Mater. Sci. **111**, 218 (2016).

[59] S. P. Huber, S. Zoupanos, M. Uhrin, L. Talirz, L. Kahle, R. Häuselmann, D. Gresch, T. Müller, A. V. Yakutovich, C. W. Andersen *et al.*, AiiDA 1.0, a scalable computational infrastructure for automated reproducible workflows and data provenance, Sci. Data **7**, 300 (2020).

[60] M. Uhrin, S. P. Huber, J. Yu, N. Marzari, and G. Pizzi, Workflows in AiiDA: Engineering a high-throughput, event-based engine for robust and modular computational workflows, Comput. Mater. Sci. **187**, 110086 (2021).

[61] P. Sc. H. Ghosez, X. Gonze, and J. P. Michenaud, *ab initio* phonon dispersion curves and interatomic force constants of barium titanate, Ferroelectrics **206**, 205 (1998).

[62] Ph. Ghosez, E. Cockayne, U. V. Waghmare, and K. M. Rabe, Lattice dynamics of BaTiO$_3$, PbTiO$_3$, and PbZrO$_3$: A comparative first-principles study, Phys. Rev. B **60**, 836 (1999).

[63] M. Paściak, S. E. Boulfelfel, and S. Leoni, Polarized cluster dynamics at the paraelectric to ferroelectric phase transition in BaTiO$_3$, J. Phys. Chem. B **114**, 16465 (2010).

[64] H. T. Stokes, D. M. Hatch, and B. J. Campbell, Isodistort, isotropy software suite, https://iso.byu.edu/ (2021).

[65] B. J. Campbell, H. T. Stokes, D. E. Tanner, and D. M. Hatch, Isodisplace: a web-based tool for exploring structural distortions, J. Appl. Crystallogr. **39**, 607 (2006).

[66] R. E. Cohen and H. Krakauer, Lattice dynamics and origin of ferroelectricity in BaTiO$_3$: Linearized-augmented-plane-wave total-energy calculations, Phys. Rev. B **42**, 6416 (1990).

[67] R. Armiento, B. Kozinsky, G. Hautier, M. Fornari, and G. Ceder, High-throughput screening of perovskite alloys for piezoelectric performance and thermodynamic stability, Phys. Rev. B **89**, 134103 (2014).